Chemical Science

ROYAL SOCIETY OF CHEMISTRY

EDGE ARTICLE

View Article Online
View Journal

Cite this: DOI: 10.1039/d5sc08479b

All publication charges for this article have been paid for by the Royal Society of Chemistry

In situ X-ray diffraction investigation of NiS_x-formation on Ni-foam using chemical vapor deposition with H_2S

Soffi Ester Sola Olesen,[ab] Magnus Kløve,[a] Anders Bæk Borup,[a] Andreas Dueholm Bertelsen,[a] Marcus Viktor Kragh-Schwarz,[bc] Thorbjørn Erik Køppen Christensen,[de] Frederik Holm Gjørup,[ad] Mads Ry Vogel Jørgensen,[ad] Jacopo Catalano,*[c] Anders W. Jensen[b] and Bo B. Iversen*[a]

Nickel foam treated *via* chemical vapor deposition (CVD) with H_2S has demonstrated potential in applications such as supercapacitors and catalysis for alkaline water electrolysis. However, the formation mechanism of the nickel sulfide surface layer remains poorly understood. In this study, *in situ* powder X-ray diffraction (PXRD) was employed to identify the crystalline phase transformations and the reaction mechanism and assess its kinetics. Ni_3S_2 formation was investigated under industrially relevant conditions by passing 3% H_2S/Ar through Ni foam and tracking the growth of the sulfided layer in relation to thickness and time. The reduced sulfidation rate observed at low flow, extended time, and greater depths indicated strong mass transfer limitations, whereas the pronounced increase between 90 and 170 °C revealed the high activation energy of the sulfidation process. A diffusion–reaction model is proposed to describe the spatial and time evolution of the Ni_3S_2 layer growth, assuming that H_2S diffuses through the newly formed Ni_3S_2 layer before reacting at the Ni interface. The modelling results indicate that both the reaction and diffusion occur at fast rates and compete in the temperature range of 130–170 °C. Post-synthesis SEM and tomography analysis confirmed improved uniformity in nickel-sulfide layer thickness and extrusion coverage when the process is reaction limited rather than diffusion limited: either at synthesis temperatures below 130 °C or a higher flow rate at 130 °C. On the other hand, higher temperatures promote the formation of large NiS_x extrusions. These results provide insight into the effect of the synthesis parameters on the microstructure and the formation of Ni_3S_2 and NiS_x, providing fundamental physico-chemical and transport properties for process optimization and upscaling.

Received 2nd November 2025
Accepted 29th January 2026

DOI: 10.1039/d5sc08479b

rsc.li/chemical-science

1. Introduction

As global warming accelerates, the demand for clean energy increases. Efficient, affordable storage is key to managing the intermittency of wind and solar power.[1] One method is to store energy in the molecular bond of hydrogen, generated through renewable-powered electrolysis. Hydrogen can be stored and transported and then later be converted back into electricity with fuel cells, making it a flexible, scalable solution for renewable energy integration.[1,2] Hydrogen also plays a critical role in various commercial processes such as steel production or the Haber–Bosch process for ammonia synthesis, which is essential for producing fertilizers that sustain global agricultural productivity.[3] However, most hydrogen currently used is derived from fossil fuels.[3] The transition to green hydrogen depends on the development of affordable, scalable, and non-precious-metal catalysts for electrolysis.[4] An example of such a catalyst is NiS_x, which can be produced by chemical vapor deposition (CVD) by flowing H_2S over Ni foam, shown to increase the overall efficiency for alkaline water electrolysis by 18%.[5] The performance enhancement of sulfided Ni foam has been extensively investigated and is now widely attributed to electrochemically induced surface reconstruction: during operation, sulfur is progressively removed, leading to phase transformation, sulfur leaching, and partial reduction of the sulfide. These processes generate defect-rich, high-surface-area structures that govern the catalytic behavior rather than the pristine NiS_x phase itself.[5–7] Apart from being a candidate for

[a]*Center for Integrated Materials Research, Department of Chemistry and INANO, Aarhus University, Langelandsgade 140, 8000 Aarhus, Denmark. E-mail: bo@chem.au.dk*

[b]*HydrogenPro ApS, Axel Gruhns Vej 3, 8270 Højbjerg, Denmark*

[c]*Department of Biological & Chemical Engineering, Aarhus University, Aabogade 40, 8200 Aarhus N, Denmark. E-mail: jcatalano@au.dk*

[d]*MAX IV Laboratory, Lund University, Fotongatan 2, 224 84 Lund, Sweden*

[e]*Department of Applied Mathematics and Computer Science, Technical University of Denmark, Richard Petersens Plads 324, 2800 Kongens Lyngby, Denmark*

renewable energy storage solutions, nickel sulfide is also utilized in supercapacitor applications,[8] hydrogenation reactions,[9] hydrogen production *via* H_2S dissociation,[10] and the metal sulfide cycle for H_2S stream removal.[11] Thus, advancing our understanding of the CVD synthesis mechanism is important for optimizing and controlling the products to ensure optimal catalytic properties across a variety of fields.

The reaction of metals with H_2S has been studied since the 1950s.[12] H_2S is known to be poisonous to Ni-catalysts used in *e.g.* hydrogenation,[12] methanation,[10] fuel cells,[10] and steam reforming.[12–14] Efforts to elucidate the mechanism of H_2S poisoning have employed several techniques, including thermal desorption,[15] gas chromatography,[16] low-energy electron diffraction (LEED),[17–19] X-ray photoelectron spectroscopy (XPS),[20] scanning electron microscopy (STM),[21] and X-ray diffraction.[22] The studies suggest that the poisoning effect is primarily geometric rather than electronic, as the activation energy for methanation remains unchanged (100 kcal mol^{-1}) for both S-poisoned and unpoisoned Ni catalysts.[16] LEED and STM studies reveal that at higher temperatures and above specific coverage, islands of ordered structures emerge.[18,21] Chemisorption studies at 323 K with 50 ppm H_2S identified two states of H_2S: rapidly forming polysulfides on the nickel sulfide surface and more slowly forming bulk sulfides through attack of the deeper layers.[15]

Herein, *in situ* powder X-ray diffraction (PXRD) is used to study the reaction between H_2S and porous Ni foam using reaction temperatures between 70 and 170 °C and a flow of 3% H_2S/Ar gas mixture at 0.1–5 mL min^{-1} (mean velocity referred to the capillary cross-sectional area of 5×10^{-3}–0.22 m s^{-1}). Compared to previous studies, these conditions involve lower temperatures and higher H_2S concentrations, enabling the investigation of NiS_x catalyst formation. The key distinction of this study is the real-time tracking of the crystalline phase appearance and transformations during the reaction, uncovering the effects of the flow rate, temperature, and reaction time. This direct observation reveals a sulfidation pathway involving distinct transient bulk phases and rate-limiting steps that are not accessible in prior LEED/XPS studies,[17–20] which focus on ordered sulfur adlayers and adsorption changes on Ni single-crystal surfaces rather than *in situ* bulk phase evolution. The reaction is examined as a function of position on the sample, revealing significant spatial variations in the reaction dynamics. Post-synthesis, scanning electron microscopy (SEM) and tomography are used to characterize the thickness of the sulfided layer, providing complementary structural insights into the PXRD data. Finally, a diffusion–reaction model is proposed to better understand the reaction kinetics and mass transport behavior of the Ni–H_2S system. By systematically varying the reaction temperature and H_2S flow rate and by tracking the evolution of crystalline phases over time, key insights are gained into how synthesis parameters influence the NiS_x products. The physico-chemical and transport parameters in the model are calibrated with *in situ* data, and its predictive capabilities are validated against independent *ex situ* measurements of the Ni_3S_2 layer thickness. The parameter set enables preliminary evaluation of process upscaling to industrially relevant scales and provides guidelines for addressing potential chemical challenges during the upscaling process.

2. Methods

2.1. *In situ* X-ray diffraction experiments

The *in situ* PXRD experiments were performed at the DanMAX beamline at MAX IV, Lund, Sweden, utilizing a modified version of the setup described by Roelsgaard *et al.*[23] and exploiting the existing *in situ* gas setup at DanMAX.[24] A piece of Ni foam, approximately 5 mm in length, was placed in a 0.7 mm fused silica capillary. A 3% H_2S/Ar gas mixture was flown through the capillary containing the Ni-foam with flow rates between 0.1 and 5 mL min^{-1}. The reaction was initiated by heating to the desired reaction temperature, 70 to 170 °C, and by keeping the reaction temperature constant throughout the one-hour reaction time. Samples are labeled based on the reaction temperature and flow rate; for example, a sample synthesized at 170 °C with a flow rate of 0.5 mL min^{-1} is referred to as 170 °C, 0.5 mL min^{-1}. A full overview of the experiments is provided in Table S1 in the SI.

The experimental setup is shown in Fig. 1, with the reaction system depicted in Fig. 1(a) and a schematic of the gas-handling and safety system in Fig. 1(b). To ensure safe operation when working with hazardous gases like H_2S, the setup was specifically designed to mitigate risks. The safety features include two H_2S detectors controlling a pneumatic three-way valve that switches to argon gas flow, if H_2S levels exceed 30 ppm. After the 3% H_2S/Ar gas passes over the sample, it is monitored using an H_2S sensor (SulfiLogger S1-1290-40000 ppm) at the outlet and subsequently neutralized with 30 wt% industrial-grade KOH. Additional safety measures, described in detail in the SI, ensured compliance with MAX IV safety protocols, as the experiments were classified as high-risk due to the use of lethal 3% H_2S/Ar gas.

PXRD patterns were continuously collected in transmission geometry during the reactions using a wavelength of 0.35424 Å and a PILATUS3 X CdTe 2M 2D single photon counting detector placed 550 mm from the capillary. An exposure time of 1 s was used for the measurements. PXRD patterns were collected approximately 1 mm from the inlet-edge of the sample, which is referred to as "position 1". The naming of the positions is shown in Fig. 1(a). Additionally, every 15 minutes, six PXRD patterns were recorded across the length of the sample at 1 mm intervals, starting from the leading edge (position 0) and extending to 5 mm into the sample (position 5). The results from position 1 (near the inlet) are shown in brown, while those from position 5 (near the outlet) are shown in grey. The beam size was set to 0.8×1.0 mm^2 ($H \times W$), ensuring no overlap between the patterns collected along the length of the Ni foam. Slight inhomogeneities were observed among different Ni foam samples. To illustrate this variability, the refined scale of the Ni phase is provided in Fig. S2 throughout the Ni foam sample from positions 0 to 5.

Synchrotron tomography was also conducted at the DanMAX beamline. A monochromatic photon beam with an energy of 35 keV was used. The beam size was 1.3 by 1.2 mm^2 ($H \times W$). The

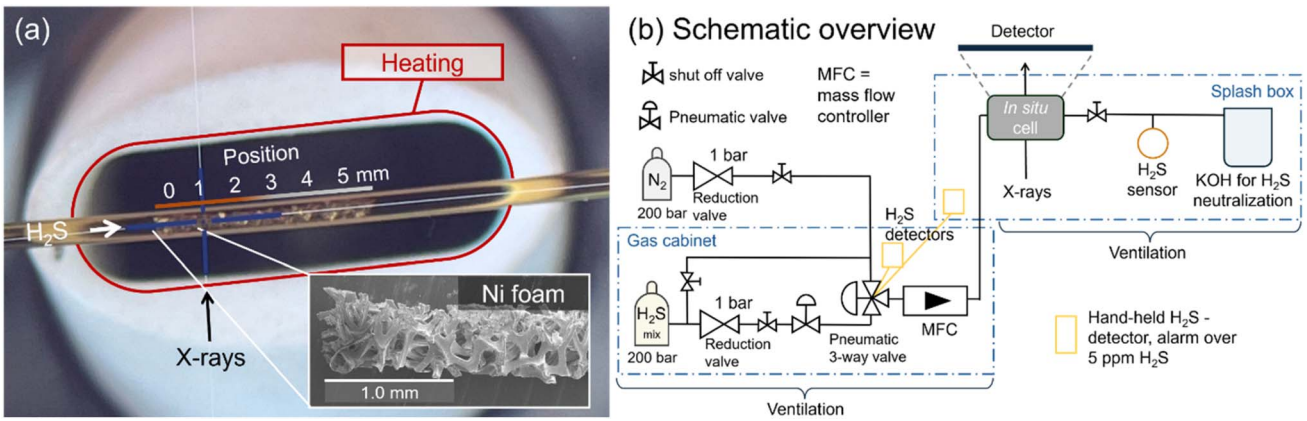

Fig. 1 (a) Image of the experimental setup, highlighting the Ni foam inside the capillary and the direction of X-rays penetrating the sample in transmission geometry. (b) Overview of the full setup including the safety system.

sample, either pristine Ni foam or sulfided Ni foam placed in the 0.7 mm fused silica capillary, was mounted on a motorized air bearing rotary stage. An sCMOS camera (Hamamatsu Orca lightning) and a ~10× objective with a high numerical aperture (Optique Peter) with a 20 μm GGG:Eu scintillator at distances of 13, 38 and 61 mm from the sample were used to collect 3002 projections of 2560 by 2092 pixels, with a pixel size of 554 nm, each with a rotation step of 0.12° between 0 and 360° using an exposure time of 100 ms per projection. 50 dark and flat field images were collected during the measurement to correct the measured projections.

2.2. Data treatment of *in situ* data

The diffraction patterns were azimuthally integrated using PyFAI.[25] All Rietveld refinements were performed using TOPAS v7.[26] For the refinements, Ni ($Fm\bar{3}m$, ICSD 8689),[27] Ni_3S_2 ($R3_2$, COD 9000564),[28] NiS ($R3m$, COD 9004078),[29] and Ni_9S_8 ($I\bar{4}2d$, COD 9013880)[30] were used. The instrumental resolution was determined for each dataset by refining Ni at the first PXRD pattern, *i.e.*, before its reaction with H_2S. The obtained peak-broadening parameters were used for analysis of the whole dataset by fixing them for subsequent refinements. Sequential Rietveld refinement was conducted in reverse order, beginning with the final frame before cooling, as it exhibited the highest Ni_3S_2 content and thus provided the best initial phase fitting. During sequential refinements, the scale factors, unit cell parameters, and the Ni_3S_2 peak broadening due to strain and crystallite size are refined. Isotropic atomic displacement parameters (ADPs) for Ni are refined as well, while they are kept constant for sulfur at a value determined at the last frame before cooling. Because sulfur constitutes only a small fraction of the total phase, its ADPs are difficult to determine reliably during the *in situ* experiments.

2.3. Data treatment of tomography data

The raw projections were normalized using an average of the collected dark and flat field images. Phase retrieval was performed using Paganin phase retrieval with a δ/β ratio of 10.[31] Data were reconstructed utilizing the gridrec algorithm[32,33] with the "cosine" filter. The tomography reconstruction process was done using DanMAX in-house software based on the Tomopy package.[34] Nickel foam and sulfided coating were segmented based on intensity thresholding using Dragonfly software (version 2024.1, build 1619).[35] Nickel foam was isolated using an intensity threshold range of [62.1, 100], while the coating was segmented from the background and foam using the intensity range [41.3, 62.1] on a calibrated intensity scale of [0, 100] for the whole volume. The foam and coating volumes were refined by performing connected component analysis to remove small groups of noisy voxels smaller than 1×10^5 voxels corresponding to a volume of $\sim 17 \times 10^3$ μm^3. Subsequent thickness analysis of the nickel foam and NiS_x coating was performed by computing the maximum inscribable sphere for the entire volume using Dragonfly.

2.4. Scanning electron microscopy energy-dispersive X-ray spectroscopy

After the *in situ* experiments, the nickel foam was analyzed with scanning electron microscopy energy-dispersive X-ray spectroscopy (SEM-ED). SEM images were recorded on a TESCAN CLARA SEM equipped with an E–T detector using 15 keV and 300 pA. The distribution of elements across the sample was determined using an EDX detector. The Aztec software from Oxford Instruments was used for quantification. To estimate the thickness of the formed NiS_x layer, SEM images were recorded before and after deliberately introducing cracks in the surface coating of the NiS_x layer.

2.5. Diffusion–reaction model of the H_2S reaction with Ni-foam

To investigate the interplay between diffusion and kinetics in the H_2S–Ni reaction, the system was modelled by considering the spatial and temporal evolution of the layer formation governed by a coupled diffusion–reaction mechanism. The model's physical–chemical and transport parameters were calibrated by using *in situ* data over a broad range of temperatures. With these parameters, the model can fully predict the NiS_x layer

growth as a function of time, temperature, and position and it was validated against independent *ex situ* measurements.

The reactor geometry was simplified as 1-D assuming a uniform velocity field through the porous media (Ni foam) and negligible gas-phase mass transfer resistance. The reaction interface was approximated as a dense, planar layer without resolving for the overlying textured layer. The model assumes that H_2S diffuses through the Ni_3S_2 layer before reacting with the underlying nickel at the Ni–Ni_3S_2 interface. Thus, the reaction boundary moves during sulfidation towards deeper layers of the solid material. A brief explanation of the model is provided below, while a comprehensive description is available in Section 3 in the SI. In the model, the sulfidation reaction is represented as a lumped pseudo first order reaction as shown in eqn (1).

$$R_{Ni_3S_2} = k_1(T) \times c^{R}_{H_2S} \quad (1)$$

where $R_{Ni_3S_2}$ is the reaction rate, $k_1(T)$ is the first order reaction coefficient, and $c^{R}_{H_2S}$ is the H_2S concentration at the Ni–Ni_3S_2 interface. The mass transfer in the thin layer is considered dominated by pure diffusion, as described by eqn (2):

$$N''_{H_2S} = h_m \times \left(c^{int}_{H_2S} - c^{R}_{H_2S}\right) = \frac{D_{H_2S-NiS_x}(T)}{\delta} \times \left(c^{int}_{H_2S} - c^{R}_{H_2S}\right) \quad (2)$$

where N''_{H_2S} is the H_2S flux through the layer, h_m is the mass transfer coefficient, $D_{H_2S-NiS_x}(T)$ is the temperature dependent diffusion coefficient of H_2S in the Ni_3S_2 layer, δ is the thickness of the sulfided layer and $c^{int}_{H_2S}$ is the concentration of H_2S at the gas-Ni interface. All variables in eqn (1) and (2), except for the kinetic and transport properties k_1, h_m, and $D_{H_2S-Ni_3S_x}$, depend on space and time. However, their explicit dependence has been omitted for clarity in the nomenclature. The parameters $D_{H_2S-NiS_x}(T)$, $k_1(T)$ and the kinetic activation energy E_a in the model are calibrated by fitting the *in situ* data.

By considering that the layer of formed Ni_3S_2 is thin, as in the thin-film approximation,[36] eqn (1) and (2) can be equated once scaled by the specific surface area of the Ni foam, P, which is the effective area for unit length scaled by the H_2S stoichiometric coefficient, thus yielding eqn (3):

$$\frac{D_{H_2S-NiS_x}(T)}{\delta} \times \left(c^{int}_{H_2S} - c^{R}_{H_2S}\right) = k_1(T) \times c^{R}_{H_2S} \times P \quad (3)$$

Eqn (3), along with the H_2S mass balance (in its differential form), forms the basis for the formulation of the partial differential equation system reported in the SI (Section 3). This system can be integrated to obtain the space and time profiles of the Ni_3S_2 layer thickness. Eqn (3) shows the explicit temperature-dependence of the diffusion and the first order kinetic coefficients, which in the present work was considered to follow an Arrhenius behaviour.

To illustrate the relative influence of the resistance of the reaction on the total resistance, eqn (3) can be rearranged to eqn (4):

$$\phi = \frac{1}{1 + \frac{k_1 \times P}{h_m}} = \frac{1}{1 + \frac{k_1 \times P}{D_{H_2S-NiS_x}} \times \delta} \quad (4)$$

where $\phi \in [0, 1]$ is a dimensionless parameter that describes the regime of the diffusion–reaction system as a function of the first Damköhler number, $Da_I = \frac{k_1 \times P}{h_m}$, which expresses the ratio between the reaction rate and the diffusive mass transfer rate. When the reaction rate and the mass transfer rate are equal ($Da_I = 1$) the resistance for the diffusion exactly balances the equivalent resistance of the pseudo-first order reaction and results in $\phi = 0.5$. This value is therefore the boundary of the two regimes. At high values of ϕ the system is reaction-limited, whereas at low values of ϕ the system becomes diffusion-limited.

3. Results and discussion

The results of analyzing the PXRD data from the sample 130 °C, 0.5 mL min^{-1} are shown in Fig. 2. Fig. 2(a) presents the raw PXRD diffractograms as a heatmap, where 2θ is plotted on the x-axis, time is on the y-axis, and the color represents the logarithmic diffraction intensity. From the heatmap, it is evident that diffraction peaks corresponding to Ni_3S_2 gradually emerge over the course of the experiment. The diffractogram collected after 60 minutes of synthesis clearly confirms the formation of Ni_3S_2 on the Ni foam, with all peaks described by either the Ni phase or the Ni_3S_2 phase, as seen from Fig. 2(b). No other phases are observed, which align with similar experiments of H_2S reacting with Ni, where only Ni_3S_2 is observed.[8,37] The nickel sulfide phase formed is governed by sulfur activity: low sulfur activity stabilizes Ni-rich phases, whereas higher sulfur activity favors sulfur-richer phases. Accordingly, in the Ni–S system, Ni_3S_2 is the thermodynamically stable phase at the Ni-rich end.[38] Combined with H_2 generation during sulfidation, which lowers the local sulfur potential, this favors formation of Ni_3S_2 over more sulfur rich phases NiS or NiS_2 at 90–170 °C.[39] Although a very thin interfacial boundary layer between Ni and Ni_3S_2 may exist, the rapid appearance of Ni_3S_2 indicates direct nucleation, consistent with closely related systems where Ni_3S_2 forms without any experimentally reported boundary layer.[7,37,40] Throughout this study, diffractograms are often shown with the logarithm of the intensity on the y-axis. This is done to provide a clearer comparison of the signal ratios between the Ni and the synthesized NiS_x, as the signal from the NiS_x phases is typically very weak. To illustrate this, a version of Fig. 2(b) is included in SI Section 2 with the data presented on a linear scale instead of the log scale. Fig. 2(c) shows the weight fraction (WF) of the Ni and Ni_3S_2 as a function of time obtained from Rietveld refinement, where Ni_3S_2 is increasing during the whole experiment. SEM images of the sample at position 1 reveal the formation of a sulfided surface layer on the Ni foam, characterized by unique extrusions, as seen in Fig. 2(d). In Section 1 in the SI, additional SEM images are shown together with EDX data.

The sulfided layer grows by consuming some of the Ni foam, as the Ni foam is the only Ni source available. From the *in situ* experiments, it appears that Ni_3S_2 is forming directly; however, due to the limitation of PXRD and the very dominant Ni peaks, potential amorphous phases forming during the reaction cannot be identified in this setup.

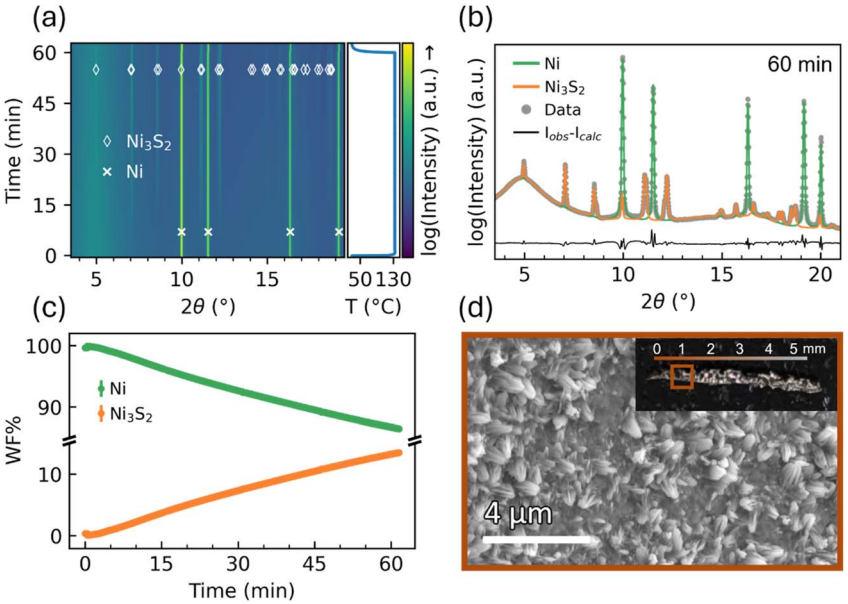

Fig. 2 Sample 130 °C, 0.5 mL min^{-1} at position 1 (1 mm from the H_2S inlet on the sample). (a) Experimental PXRD patterns of the *in situ* experiment represented as a heatmap. (b) Refined PXRD pattern 60 min after the synthesis is initiated by heating. (c) WF% of Ni_3S_2 and Ni as a function of time. (d) SEM image of the inlet of H_2S (position 1) after synthesis.

3.1. Effect of temperature

The influence of synthesis temperature in the range of 70–170 °C using a flow rate of 0.5 mL min^{-1} on the WF% of Ni_3S_2 is studied at position 1. At 70 °C in the heatmaps of the raw data in Section 2 of the SI, the Ni_3S_2 phase is absent, indicating that a lower minimum temperature for Ni_3S_2 formation exists. Increasing the temperature incrementally from 90 to 170 °C increases the amount of Ni_3S_2 phase formed at position 1, as seen in Fig. 3(a). The results from the diffusion–reaction model are shown as black continuous lines in Fig. 3(a). A schematic of the model is shown in Fig. 3(b); see Section 3 in the SI for a detailed explanation of the optimization algorithm and calculation of the numerical standard deviations. The best fit of the *in situ* data provides the diffusion coefficient for H_2S through the Ni_3S_2 layer of $D_{H_2S\text{–}NiS_x}^{T_{ref}} = 2 \times 10^{-13}$ m^2 s^{-1} and the pseudo-first order kinetics of $k_1^{T_{ref}} = (3.4 \pm 0.1) \times 10^{-8}$ s^{-1}, both at the reference temperature of 25 °C, and an activation energy for the pseudo first order reaction of H_2S with Ni of $E_a = 65.3 \pm 0.3$ kJ mol^{-1}. For comparison, sulfidation of Ni in similar studies was reported to result in activation energies of around 90 kJ mol^{-1},[41,42] while sulfidation of Cu and Cu–Ni alloys (10 and 50 wt% Ni) was reported to result in activation energies of 71 and 40 kJ mol^{-1}, respectively.[43]

The H_2S diffusion coefficient is comparable to that of *e.g.* H_2 gas through (structured) Ni and Ni–P coatings, ~1–4 × 10^{-13} m^2 s^{-1} and ~3 × 10^{-13}–2 × 10^{-12} m^2 s^{-1}.[44] In contrast, Ni self-diffusion through Ni_3S_2 is unlikely, with reported values near 10^{-14} m^2 s^{-1} at 450 °C,[45] extrapolating to ~10^{-20} m^2 s^{-1} at 100 °C. Moreover, the diffusion of Ni in metallic Ni is even slower, measured below 10^{-22} m^2 s^{-1} at 700 °C.[46]

It should be stressed that, although the experiments were conducted in a small capillary, the calibrated physico-chemical and transport properties have broader relevance. Since mass transfer occurs within the porous medium, whose characteristic length is in the hundreds of micrometers, the reported parameters can be applied to derive mass-transfer correlations and scaling relationships for process upscaling.

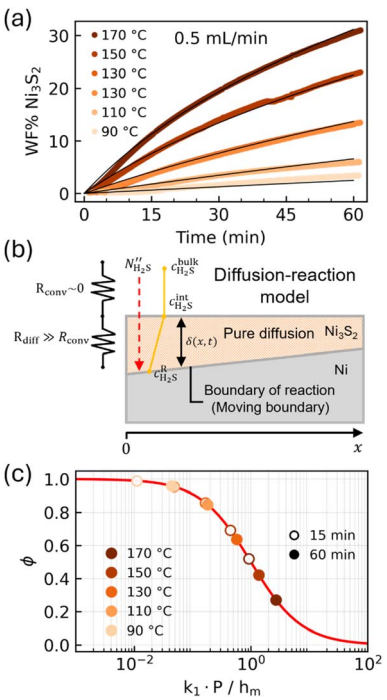

Fig. 3 Samples at position 1. (a) Weight fraction of Ni_3S_2 as a function of time synthesized with a flow of 0.5 mL min^{-1} and at reaction temperatures of 90–170 °C with the fitted model shown in black. (b) Model of H_2S diffusion through the Ni_3S_2 layer and reacting with Ni. (c) Relative influence, ϕ of the reaction on the total resistance at position 1 for 15 min in open circles, ○, and 60 min in filled circles, ●.

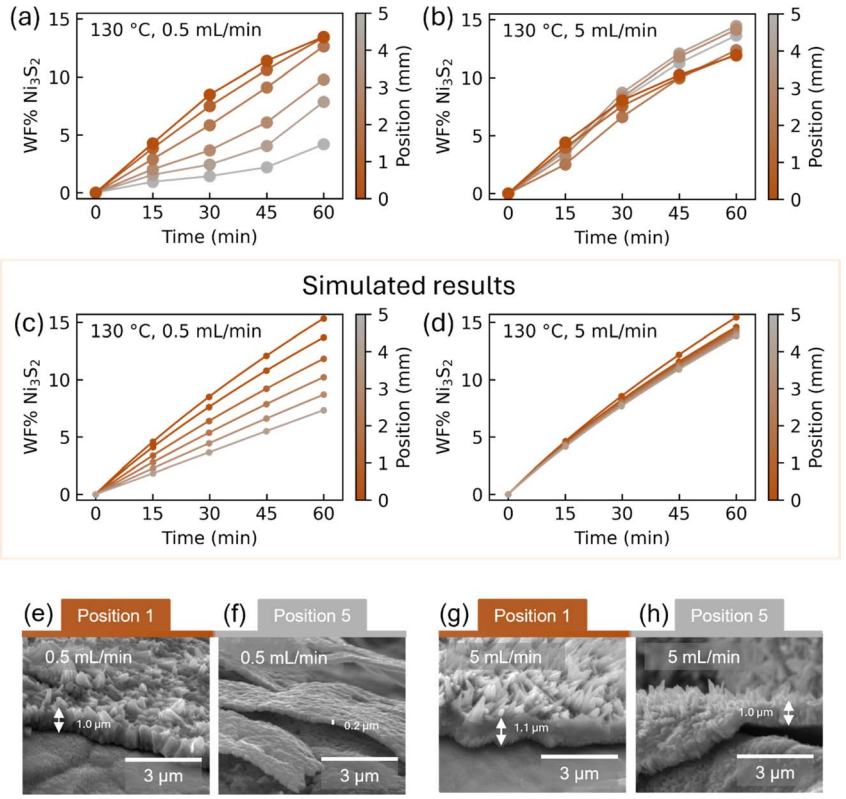

Fig. 4 Weight fraction of Ni_3S_2 from *in situ* PXRD as a function of synthesis time at 5 different positions across the Ni foam sample for 130 °C with flow rates of (a) 0.5 mL min^{-1} and (b) 5 mL min^{-1}. Simulated results with the diffusion–reaction model at (c) 0.5 mL min^{-1} and (d) 5 mL min. (e–h) SEM images of synthesized Ni-foams cut with a scalpel, thus inducing cracks to showcase the thickness of the formed Ni_3S_2 layer for sample 0.5 mL min^{-1} at (e) position 1 and (f) position 5 and for sample 5 mL min^{-1} at (g) position 1 and (h) position 5.

As the Ni_3S_2 layer thickens, the reaction becomes increasingly constrained by the diffusion of H_2S through this layer, as illustrated in Fig. 3(b). To evaluate the impact of mass transfer resistance, the dimensionless parameter ϕ, eqn (4), which represents the relative contribution of the reaction to the overall resistance, is presented for reaction times of 15 and 60 minutes in Fig. 3(c). A high value of ϕ means that the system is reaction limited, while at low values, the system is diffusion limited. At 170 °C, ϕ drops to 0.5 within 15 minutes, indicating that the process becomes predominantly diffusion-limited rather than reaction-limited at long reaction times. The diffusion limitation arises because of the resistance for H_2S to permeate the already-formed NiS_x layer. As the layer thickness increases, so does the resistance for diffusion, resulting in an overall reaction mechanism which is increasingly diffusion-limited. Thus, lowering the reaction temperature delays the tip-over point for when the reaction becomes diffusion limited. For example, for the 130 °C sample, it only starts to reach the same diffusion limitation after 60 minutes, when ϕ is close to 0.6.[43]

3.2. Effect of temperature and flow on lateral positions

Every 15 minutes during the *in situ* experiments, PXRD patterns were collected along the length of the sample, enabling assessment of the progression of the CVD synthesis across the sample. Fig. 4(a) and (b) show the WF% of Ni_3S_2 as a function of time for the samples synthesized at 130 °C at 0.5 mL min^{-1} and 5 mL min^{-1}, respectively. The position from the inlet of H_2S is marked with a color ranging from brown to grey. For 5 mL min^{-1}, the refined WF% values of all positions are almost the same, indicating homogeneity across the entire sample. For 0.5 mL min^{-1}, on the other hand, the amount of Ni_3S_2 decreases further away from the inlet, which is confirmed with the decreased H_2S amount in the outlet gas as shown in Section 4 in the SI, suggesting that the H_2S gas has not been in sufficient excess for the reaction to produce a homogeneous sample. The results from the diffusion reaction model are shown in Fig. 4(c) and (d), showing overall similar trends compared to Fig. 4(a) and (b).

To examine the reproducibility, three samples at 130 °C with a H_2S flow of 0.5 mL min^{-1} were synthesized. The WF% of Ni_3S_2 as a function of position in Fig. S19(b) shows that they all exhibit a similar trend with lower Ni_3S_2 content at positions 4–5. To assess the effect of flow rate, samples were prepared at 130 °C with flow rates of 5, 1, 0.5, and 0.1 mL min^{-1}. As shown in Section 4 of the SI, the 0.1 mL min^{-1} experiment exhibits significantly lower Ni_3S_2 formation after 60 minutes compared to higher flow rates, indicating that H_2S availability becomes the limiting factor at low flow.

The SEM images in Fig. 4(e–h) confirm the homogeneity difference between 0.5 and 5 mL min^{-1} at 130 °C, with the 0.5 mL min^{-1} sample showing no extrusions on top of the sulfided layer at position 5. Additionally, the layer thickness measured

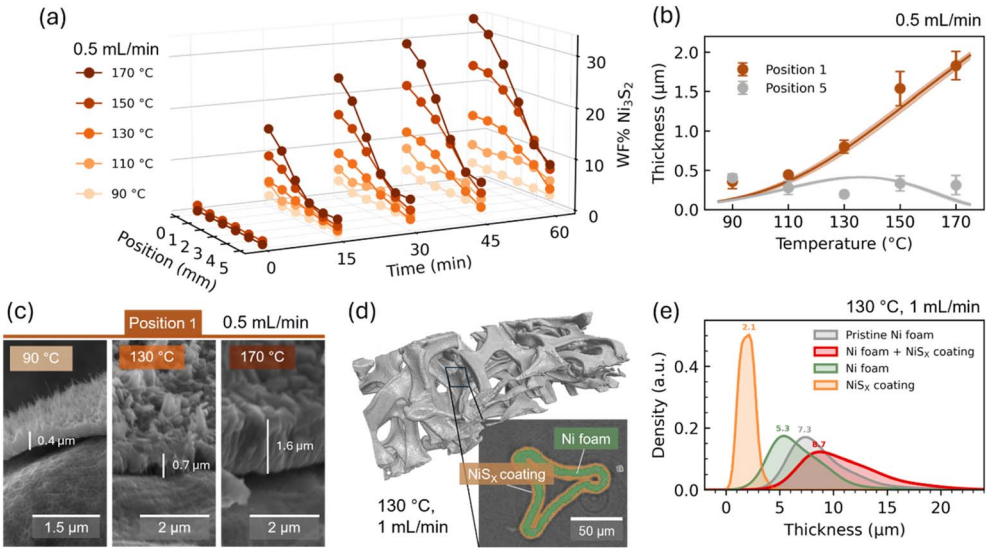

Fig. 5 (a–c) Samples at 0.5 mL min^{-1} at temperatures of 90–170 °C. (a) WF% of Ni_3S_2 determined by *in situ* PXRD as a function of reaction temperature, time, and position across the sample. (b) Average thickness of the sulfided layer at inlet position 1 and outlet position 5, with the predictions from the model represented as a solid line. Average thickness is from 3 different spots on the sample; at each spot 3 different thicknesses are measured. (c) SEM images of 0.5 mL min^{-1} samples at 90 °C, 130 °C, and 170 °C, at position 1 (inlet). (d and e) Tomography data for sample 130 °C, 1 mL min^{-1}. (d) Three-dimensional render of the reconstructed sulfided nickel foam volume with zoom-in showing a representative 2D slice of the segmented coating and nickel foam. (e) Volume thickness distribution of pristine Ni foam, the 1 mL min^{-1} sample for the Ni foam and coating combined, the Ni foam after sulfiding and the coating after sulfiding.

with SEM at position 5 is generally thinner compared to that at position 1 for the 0.5 mL min^{-1} sample. In contrast, the 5 mL min^{-1} sample has a comparable thickness of the Ni_3S_2 layer at positions 1 and 5, and extrusions on top of the layer are visible at both positions. This suggests that for upscaling of H_2S CVD on Ni foam, the regime should be reaction-limited, *i.e.* the flow rate and concentration should be sufficiently high to ensure that the samples are homogeneous.

The distribution of Ni_3S_2 across the Ni foam is influenced by temperature, mass transfer, and fluid flow. Higher temperatures predominantly increase the weight fraction of Ni_3S_2 near the H_2S inlet (positions 0 and 1), while the fraction at position 5 shows minimal change, as illustrated in Fig. 5(a). Reaction time, however, does not significantly improve uniformity within the temperature range of 130–170 °C at a flow rate of 0.5 mL min^{-1}. The increased reaction at the inlet aligns with prior studies on Ni catalyst beds, where sulfiding occurs primarily at the inlet.[47] Additionally, studies on H_2S sulfidation in packed bed reactors suggest that local heating of particles can result in severe hot spots and H_2S starvation.[48] Thus, the decreased reaction in the outlet could be related to H_2S flow through the Ni foam. Furthermore, sulfur content measurements of the outlet gas at 0.5 mL min^{-1} show a decrease in H_2S at higher temperatures as shown in SI Section 5, consistent with the lower Ni_3S_2 weight percentages observed in the outlet of high-temperature samples in Fig. 5(a). Higher flow rates may increase the local H_2S concentration at the gas/solid interface, potentially due to more reactant supply and increased turbulence, affecting the sulfur uptake and layer formation.

SEM analysis of the segmented samples at 0.5 mL min^{-1}, shown in Fig. 5(b), confirms a thicker sulfided layer at position 1 especially for higher temperature samples, as indicated in Fig. 5(a), with a significantly thinner layer observed at position 5. Fig. 5(b) also shows the model predictions, which agree well with the experimental data. However, the model slightly underestimates the layer thickness at 90 °C, as seen in Fig. 5(a). The thickness of the sulfided layer at position 1 is 0.80(8) µm at 130 °C and 1.8(2) µm at 170 °C, corresponding to a 2.2-fold increase in thickness. These values are comparable to those of a previous larger-scale study, which reported a thickness of ~1 µm after 2 h at 110 °C.[5] The Ni_3S_2 weight fraction at position 1 shows a similar increase of 2.4 times, with a 13.4(2) WF% at 130 °C and 31(2) WF% at 170 °C.

As shown in Fig. 4, increasing the flow rate enhances the uniformity of Ni_3S_2 distribution throughout the sample. However, enhanced uniformity can also be achieved at lower temperatures (90 °C and 110 °C) with a flow rate of 0.5 mL min^{-1}, as illustrated in Fig. 5(b). Thus, for industrial-scale applications, higher flow rates or lower temperatures are recommended to achieve uniform Ni_3S_2 deposition. For more precise determination of temperature and flow limits in a larger-scale reactor, the extracted kinetic and diffusion parameters may be combined with reactor-scale fluid dynamics and porous-media mass transport to provide guideline predictions, which can subsequently be expressed through standard dimensionless correlations for different reactor geometries.

The tomographic reconstruction and corresponding 2D cross-sectional view in Fig. 5(d) clearly reveal that the NiS_x coating forms as an outer layer on the Ni foam structure. The volume thickness distributions in Fig. 5(e) show that the pristine Ni foam has a smaller layer thickness compared to the sulfided sample, which includes both the Ni foam and the NiS_x

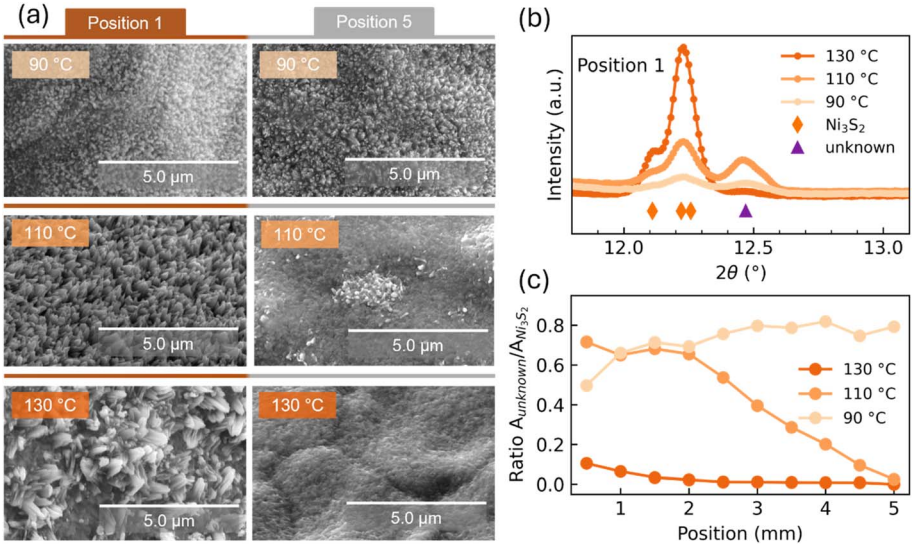

Fig. 6 Samples at 0.5 mL min^{-1} flow at temperatures of 90 °C, 110 °C, and 130 °C after synthesis. (a) SEM from positions 1 and 5 of the samples. (b) Diffractogram in a selected range of 2θ values with Ni_3S_2 peaks and peaks from the unknown phase. (c) Ratio of area of peaks from single peak fitting of Ni_3S_2 peaks and unknown peaks shown in (b) as a function of position.

coating. The reduced thickness of the Ni foam after sulfidation, excluding the coating, is expected, as some of the Ni is consumed in forming the NiS_x layer. The sulfided coating displays a well-defined thickness distribution ranging from 0–4 µm with an average thickness of 2.0(6) µm. The thickness exceeds the voxel size of 0.554 µm, confirming that the measurement is not resolution-limited. The average thickness of sulfided coating from tomography is higher than that obtained from SEM in a comparable 130 °C sample (Fig. 4g and h). However, unlike SEM, where only the dense coating layer is measured, tomography includes both the dense layer and the surface extrusions, contributing to a higher apparent thickness. For comparison the surface extrusions were estimated on the SEM images to be around 0.7–0.9 µm, which could make up for the difference of 0.9–1 µm in SEM and tomography. Accurate thickness estimation *via* tomography requires careful tuning of experimental parameters. For instance, increasing the sample-to-detector distance enlarges phase fringes, which can obscure signals from thin layers such as the sulfided coating. The data in Fig. 5(d) were acquired at a 13 mm distance; at larger distances (38 mm and 61 mm) fringe size became excessive, preventing reliable measurements (data not shown).

For more precise thickness quantification, holographic tomography[49] or ptychographic imaging[50] could be employed as they better account for coherent effects, although at the expense of a smaller field of view. However, these techniques are beyond the scope of this work.

3.3. Surface morphology and additional phases

SEM images of the H_2S inlet and outlet (positions 1 and 5) in Fig. 6(a) illustrate that lower temperatures result in a more uniform morphology at a flow rate of 0.5 mL min^{-1} at 90–130 °C. At 90 °C, the surface morphology is consistent at both positions, characterized by small extrusions. This morphology is consistent with previous reports on H_2S sulfiding of metals, which describe a dense inner layer and an outer layer composed of extrusions.[51] At 110 °C, similar small extrusions are observed at position 1, but there are significantly fewer extrusions present at position 5, forming small islands. This observation aligns with previous reports, which describe the emergence of islands when using higher synthesis temperatures in ultra-high vacuums, specifically above 227 °C in one investigation[21] and 327 °C in another.[19] The 130 °C sample exhibits larger extrusions at position 1, with no extrusions present at position 5. Additional SEM images for positions 1 and 5 across all temperatures in Section 6 in the SI corroborate the observed trend: higher temperatures result in no extrusions at position 5 and increasingly larger extrusions at position 1. As higher surface area increases both water electrocatalysis and supercapacitor performance,[52,53] the impact of extrusion size on these performances could be interesting for further study; however, it lies beyond the scope of this work.

The PXRD patterns in Fig. 6(b) reveal a peak at $2\theta = 12.46°$ for sample 90 °C and 110 °C, which does not correspond to the known phases of Ni or Ni_3S_2. In the PXRD pattern in Section 6 in the SI, an additional peak at $2\theta = 7.5°$ is observed. A study of the Ni reaction with H_2S at 390–550 °C describes a mechanism of the inner layer of Ni_3S_2 with NiS of both the millerite and the nickel arsenide structure formed on top. Additionally, small amounts of α-Ni_7S_6 and β-Ni_7S_6 are observed.[22] Section 6 in the SI explores whether these peaks could be attributed to any other NiS_x phases with an overview provided in Table S4, but no matching phase was identified, neither NiS nor Ni_7S_6. Furthermore, in Section 6 in the SI, PXRD patterns of samples at higher flow rates of 1 and 5 mL min^{-1} show that a new unidentified phase is present after synthesis, which is seemingly having peaks at the same positions as the unknown phase in 90 °C and 110 °C samples.

The surface coverage of extrusions at 90 °C and 110 °C may be linked to this additional phase. Since the unidentified phase could not be associated with any known phases (Section 6 in the SI), the unknown peak at $2\theta = 12.48°$ was analyzed using single-peak fitting alongside the Ni_3S_2 peaks at lower 2θ values, as shown in Fig. 6(b). The ratio of the unknown peak area to the adjacent Ni_3S_2 peaks, presented in Fig. 6(c), indicates that the weight fraction of the unidentified phase remains constant across the 90 °C sample. However, it decreases towards position 5 for the 110 °C sample, correlating with the morphology changes in Fig. 6(a) and the color change in Fig. S29.

The appearance of the NiS millerite phase in 150 °C and 170 °C samples with the WF% at around 1.5% NiS millerite at position 0 is indicated in Section 6 in the SI. Previous *ex situ* synthesis in a tube furnace demonstrated an increase in NiS millerite WF% with longer synthesis times.[5] A literature study reports that with sulfiding below the eutectic temperature of Ni_3S_2–Ni at 670 °C the layer will consist of a thick inner layer of Ni_3S_2 and a thin outer layer of NiS,[20,22] which indicates that the extrusions on top of sample 170 °C positions 0 and 1, identified with SEM, can be attributed to the NiS phase, as discussed in Section 6.3 in the SI. Furthermore, the proportion of NiS is suggested to depend on the concentration of H_2S.[20] The literature suggests that Ni_3S_2 is not the most thermodynamically stable phase, with NiS and Ni_7S_6 being more stable.[54,55] Combined with the literature indicating that the Ni_3S_2 to NiS transformation requires substantial energy,[56] this suggests that extended synthesis durations are needed to observe and study this phase transition.

4. Conclusions

This study provides new insights into the sulfidation of Ni foam with H_2S. *In situ* PXRD revealed that the reaction of H_2S on Ni foam resulted in the formation of NiS_x phases, primarily Ni_3S_2. The growth of the Ni_3S_2-phase was influenced by reaction temperature and the gas flow rate, with higher temperatures increasing the weight fraction of Ni_3S_2 at the sample inlet. No reaction occurred at 70 °C within 60 min, which enabled locating the lower-bound temperature for layer formation between 70 and 90 °C. Lower flow rates localized the reaction at the inlet, while higher flow rates produced a uniform Ni_3S_2 layer across the sample.

Analysis of sulfided layer thickness *via* SEM at multiple positions and temperatures enabled the formulation of a diffusion–reaction model, estimating the Ni_3S_2 formation activation energy at about 65 kJ mol^{-1}. The model shows that diffusion control dominates at higher temperatures and longer reaction times. Layer uniformity and extrusion coverage were improved when working in the reaction-limited region, *e.g.* by either lowering the synthesis temperature or increasing the H_2S flow rate at 130 °C.

The formation of NiS_x on Ni foam has among other things been shown to improve the overall efficiency for alkaline water electrolysis compared with Ni foam. Due to its simple synthesis method, upgrading Ni foam to NiS_x may be of industrial relevance, and this work establishes a fundamental understanding of key process parameters for industrial CVD-production of nickel sulfide electrodes using H_2S, paving the way for its upscaling.

Author contributions

Conceptualization: SESO, AWJ, MRVJ, JC, BBI; investigation: SESO, MK, ABB, AD, MVKS, TEKC, FHG; formal analysis: SESO, MK, ABB, AD, MVKS, TEKC, FHG, JC; methodology: SESO, JC, MK, ABB, AD, TEKC; resources: AWJ, JC, BBI; supervision: AWJ, JC, MRVJ, BBI; writing – original draft: SESO, JC; writing – review and editing: SESO, MK, ABB, AD, MVKS, TEKC, FHG, MRVJ, AWJ, JC, BBI.

Conflicts of interest

There are no conflicts to declare.

Data availability

Data supporting this article have been included as part of the supplementary information (SI). Additional data of this study are available from the corresponding author upon reasonable request. Supplementary information is available. See DOI: https://doi.org/10.1039/d5sc08479b.

Acknowledgements

This study was supported by the Villum Foundation (25861), the Danish National Research Foundation (DNRF189), the Carlsberg Foundation, Innovation Fund Denmark Industrial PhD number 3129-00005B and EUDP 640222-496379. We thank the Danish Agency for Science, Technology, and Innovation for funding the instrument center DanScatt. We acknowledge MAX IV Laboratory for time on DanMAX under proposal 20231613 and thank the safety team for help in creating a safe environment to work with H_2S. Research conducted at MAX IV, a Swedish national user facility, was supported by the Swedish Research Council under contract 2018-07152, the Swedish Governmental Agency for Innovation System under contract 2018-04969, and Formas under contract 2019-02496. DanMAX is funded by the NUFI grant no. 4059-00009B. The Carlsberg Foundation is acknowledged for funding the Tescan Clara SEM used in this work. Furthermore, the Innovation Fund Denmark is acknowledged for funding through the H2-FOAM Grand Solution grant no. 3148-00011B.

Notes and references

1 I. Dincer and C. Acar, *Int. J. Hydrogen Energy*, 2015, **40**, 11094–11111.
2 S. Ould Amrouche, D. Rekioua, T. Rekioua and S. Bacha, *Int. J. Hydrogen Energy*, 2016, **41**, 20914–20927.
3 M. Wang, M. A. Khan, I. Mohsin, J. Wicks, A. H. Ip, K. Z. Sumon, C.-T. Dinh, E. H. Sargent, I. D. Gates and M. G. Kibria, *Energy Environ. Sci.*, 2021, **14**, 2535–2548.

4 A. A. Feidenhans'l, Y. N. Regmi, C. Wei, D. Xia, J. Kibsgaard and L. A. King, *Chem. Rev.*, 2024, **124**, 5617–5667.
5 S. E. S. Olesen, A. W. Jensen, M. Kløve, F. Fenini, J. Nissen, B. B. Iversen, A. Bentien and L. P. Nielsen, *ACS Catal.*, 2024, 11931–11940.
6 K. Kawashima, A. E. F. Milton, J. S. Archer, D. T. Collins, N. L. Serrat, C. E. Chukwuneke, R. A. Marquez, L. A. Smith and C. B. Mullins, *ACS Energy Lett.*, 2024, **9**, 6126–6143.
7 S. Haghverdi Khamene, N. van Dalen, M. Creatore and M. N. Tsampas, *ChemSusChem*, 2025, e202501880.
8 Y. Q. Cao, X. Qian, W. Zhang, M. Li, S. S. Wang, D. Wu and A. D. Li, *Electrochim. Acta*, 2019, **303**, 148–156.
9 A. Olivas, J. Cruz-Reyes, V. Petranovskii, M. Avalos and S. Fuentes, *J. Vac. Sci. Technol., A*, 1998, **16**, 3515–3520.
10 A. Zagoruiko, *Catal. Today*, 2019, **329**, 171–176.
11 O. Osasuyi, D. V. Quang, G. Basina, Y. Al Wahedi, M. R. M. Abu Zahra, G. Palmisano and K. Al-Ali, *Ind. Eng. Chem. Res.*, 2022, **61**, 6135–6145.
12 C. H. Bartholomew, *Stud. Surf. Sci. Catal.*, 1987, **34**, 81–104.
13 S. L. Lakhapatri and M. A. Abraham, *Catal. Sci. Technol.*, 2013, **3**, 2755.
14 Y. Chen, C. Xie, Y. Li, C. Song and T. B. Bolin, *Phys. Chem. Chem. Phys.*, 2010, **12**, 5707.
15 P. Marécot, E. Paraiso, J. M. Dumas and J. Barbier, *Appl. Catal., A*, 1992, **20**, 89–97.
16 W. D. Fitzharris, J. R. Katzer and W. H. Manogue, *J. Catal.*, 1982, **76**, 369–384.
17 T. Edmonds, J. J. McCarroll and R. C. Pitkethly, *J. Vac. Sci. Technol.*, 1971, **8**, 68–74.
18 W. Erley and H. Wagner, *J. Catal.*, 1978, **53**, 287–294.
19 J. N. Andersen, *Surf. Sci.*, 1987, **192**, 583–596.
20 K. T. Ng and D. M. Hercules, *J. Phys. Chem.*, 1976, **80**, 2094–2102.
21 F. Besenbacher, P. T. Sprunger, L. Ruan, L. Olesen, I. Stensgaard and E. Lægsgaard, *Top. Catal.*, 1994, **1**, 325–341.
22 N. W. Tideswell, *Corrosion*, 1972, **28**, 23–25.
23 M. Roelsgaard, M. Kløve, R. Christensen, A. D. Bertelsen, N. L. N. Broge, I. Kantor, D. R. Sørensen, A. C. Dippel, S. Banerjee, M. V. Zimmermann, P. Glaevecke, O. Gutowski, M. R. V. Jørgensen and B. B. Iversen, *J. Appl. Crystallogr.*, 2023, **56**, 581–588.
24 T. R. Jensen, T. K. Nielsen, Y. Filinchuk, J.-E. Jørgensen, Y. Cerenius, E. M. A. Gray and C. J. Webb, *J. Appl. Crystallogr.*, 2010, **43**, 1456–1463.
25 J. Kieffer, V. Valls, N. Blanc and C. Hennig, *J. Synchrotron Radiat.*, 2020, **27**, 558–566.
26 A. A. Coelho, *J. Appl. Crystallogr.*, 2018, **51**, 210–218.
27 V. I. Voronin, I. F. Berger, N. V. Proskurnina and B. N. Goschitskii, *Phys. Met. Metallogr.*, 2016, **117**, 348–354.
28 M. E. Fleet, *Am. Mineral.*, 1877, **62**, 341–345.
29 J. D. Grice and R. B. Ferguson, *Can. Mineral.*, 1974, **12**, 248–252.
30 S. Merlino and E. Makovicky, *Eur. J. Mineral.*, 2009, **21**, 863–869.
31 D. Paganin, S. C. Mayo, T. E. Gureyev, P. R. Miller and S. W. Wilkins, *J. Microsc.*, 2002, **206**, 33–40.
32 B. A. Dowd, G. H. Campbell, R. B. Marr, V. V. Nagarkar, S. V. Tipnis, L. Axe and D. P. Siddons, in *Developments in X-Ray Tomography II*, ed. U. Bonse, Denver, CO, United States, 1999, pp. 224–236.
33 M. L. Rivers, in *Developments in X-Ray Tomography VIII*, ed. S. R. Stock, San Diego, California, United States, 2012, p. 85060U.
34 D. Gürsoy, F. De Carlo, X. Xiao and C. Jacobsen, *J. Synchrotron Radiat.*, 2014, **21**, 1188–1193.
35 *Dragonfly 3D World (Version 2024.1)*, Comet Technologies Canada Inc., Montreal, 2024, https://dragonfly.comet.tech/.
36 R. Bird, W. Stewart and E. Lightfoot, *Transport Phenomena*, John Wiley and Sons, New York, 2nd edn, 2002.
37 T. A. Ho, C. Bae, H. Nam, E. Kim, S. Y. Lee, J. H. Park and H. Shin, *ACS Appl. Mater. Interfaces*, 2018, **10**, 12807–12815.
38 H. Gamsjäger, J. Bugajski, T. Gajda, R. J. Lemire and W. Preis, *Chemical Thermodynamics of Nickel*, Elsevier Science, 2005, vol. 6.
39 S. Cristol, J. F. Paul, E. Payen, D. Bougeard, S. Clémendot and F. Hutschka, *J. Phys. Chem. B*, 2000, **104**, 11220–11229.
40 L. Peng, C. Wang, C. Q. Wang, R. Shi, T. Zhang and G. I. N. Waterhouse, *Adv. Energy Sustainability Res.*, 2021, **2**, 2100078.
41 S. Mrowec and K. Przybylski, *High Temp. Mater. Process.*, 1984, **6**, 1–80.
42 L. Czerski, S. Mrowec and T. Werber, *J. Electrochem. Soc.*, 1962, **109**, 273.
43 B. Chattopadhyay and S. Sadigh-Esfandiary, *Corros. Sci.*, 1973, **13**, 747–757.
44 D. Biggio, B. Elsener and A. Rossi, *Coatings*, 2025, **15**, 365.
45 K. Fueki, Y. Oguri and T. Mukaibo, *Bull. Chem. Soc. Jpn.*, 1968, **41**, 569–572.
46 H. Mehrer, *Diffusion in Solids*, Springer Berlin Heidelberg, Berlin, Heidelberg, 1st edn, 2007, vol. 155.
47 J. Richardson, *J. Catal.*, 1971, **21**, 130–138.
48 S. C. Reyes and T. C. Ho, *AIChE J.*, 1988, **34**, 314–320.
49 P. Cloetens, W. Ludwig, J. Baruchel, D. Van Dyck, J. Van Landuyt, J. P. Guigay and M. Schlenker, *Appl. Phys. Lett.*, 1999, **75**, 2912–2914.
50 M. Holler, A. Diaz, M. Guizar-Sicairos, P. Karvinen, E. Färm, E. Härkönen, M. Ritala, A. Menzel, J. Raabe and O. Bunk, *Sci. Rep.*, 2014, **4**, 3857.
51 S. Mrowec and K. Przybylski, *High Temp. Mater. Process.*, 1984, **6**, 1–80.
52 D. E. Hall, *J. Electrochem. Soc.*, 1981, **128**, 740–746.
53 J. Meena, S. S. Sivasubramaniam, E. David and S. K, *RSC Sustain.*, 2024, **2**, 1224–1245.
54 M. Arita, *Metall. Mater. Trans. A*, 2006, **37**, 3009–3022.
55 L. Cemic and O. J. Kleppa, *Geochim. Cosmochim. Acta*, 1986, **50**, 1633–1641.
56 H. Kiuchi, K. Funaki, Y. Nakai and T. Tanaka, *Int. J. Hydrogen Energy*, 1984, **9**, 701–705.